Particle Simulation of Near-Surface Cusp Confinement of Weakly Ionized Plasma

IEPC-2013-349

Presented at the 33rd International Electric Propulsion Conference,
The George Washington University, Washington, D.C., USA
October 6–10, 2013

Samuel J. Araki* and Richard E. Wirz†
University of California, Los Angeles, CA, 90095, USA

An iterative Monte-Carlo model is developed to investigate near-surface dynamics and structure of plasma for a single permanent magnetic cusp. Improved understanding in this region will allow electric propulsion designers to take advantage of cusp confinement for micro-scale discharges (∼1 cm), enabling high performance micro-thrusters that are attractive for both micro-satellite and formation flying missions. The computational model has several key features desirable for this specific problem. The model uses an adaptive mesh to provide improved resolution in the cusp region; methods used for electric potential and field calculations allow second-order accurate solutions even at the coarse/fine grid interface of the adaptive mesh. The model also uses analytic equations for magnetic field calculation and improved techniques for particle advancement, which are critical in determining accurate particle trajectories very near the cusp. In this paper, a few important components of the model are validated against analytical solutions. In addition, a test simulation is performed using the computational model. Although the computational model does not provide fully converged results at this stage, the model is still capable of capturing the sheath and resolving features of the plasma very near the magnetic cusp.

Nomenclature

B	Magnetic field, T
D	Diffusion coefficient, m^2/s
E	Electric field, V/m
I	Current, A
J	Jacobian
L	Minimum dimension of a cell, m
M	Magnetization, A/m
N	Number of particles
N_c	Number of cells
P	Probability
Q	Number of values used for mixing
R	Residual
S	Cell face area, m^2
T	Temperature, eV
U	Random number between 0 and 1
V	Volume, m^3
W	Weighting factor
$\hat{h}$	Unit vector
m	Mass, kg
n	Density, 1/m^3
$\dot{n}$	Generation rate density, 1/m^3 s
q	Charge, C
r	Radial position, m
v	Velocity, m/s
w_l	Leak width, m
z	Axial position, m
Δt	Time-step, s
Γ	Particle flux, 1/m^{2}s
Λ_D	Debye length, m
χ	Deflection angle, rad
ϵ	Kinetic energy normalized by 27.21 eV
ε_0	Vacuum permittivity, F/m
η	Component in natural coordinates
μ	Mobility, m^2/V s
μ_0	Permeability of vacuum, N/A^2
ϕ	Electric potential, V
ρ	Gyroradius, m
ρ_f	Total electric charge density, C/m^3

*Graduate Student, Mechanical and Aerospace Engineering, samuel.jun.araki@ucla.edu.
†Assistant Professor, Mechanical and Aerospace Engineering, wirz@ucla.edu

σ	Collision cross-section, m^2
θ	Angle, rad
ξ	Component in natural coordinates

Subscripts

$\parallel$	Parallel
$\perp$	Perpendicular
e	Electron
el	Elastic
ex	Excitation
h	Hybrid
i	Ion
iz	Ionization
j	Cell index
k	Vertex
l	Current loop
m	Magnet
max	Maximum
n	Current time-step
o	Neutral
out	Output
p	Macro-particle
r	Radial component
rel	Relative
w	Wall
z	Axial component

I. Introduction

THE motivation for this study is to improve the understanding of cusp confinement very near the anode surface of a permanent magnet discharge, thus enabling the development of efficient micro-discharges on the order of 1 cm in diameter. A micro-scale thruster of this size is attractive for various applications, including large ΔV missions using small spacecraft,[1] and formation flying and control of larger spacecraft.[2,3] Large magnetically confined discharges ($\gtrsim$ 13 cm) benefit from relatively low surface-to-volume ratios, which can provide favorable electron confinement and high ionization efficiency. As a result, designers of many large cusp confined devices, such as ring-cusp ion thrusters, have been able to yield favorable performance for large discharges by focusing on the design of the macroscopic magnetic field structure far from the magnet surfaces.[4,5] In contrast, the permanent magnets result in strong microscopic cusp structures that dominate a large region in smaller discharges. The DC-ION model, which self-consistently included effects of high-energy (primary) electrons along with other plasma species, was scaled down to simulate the 3 cm Miniature Xenon Ion (MiXI) ring cusp thruster.[6] Results from the model confirmed inferences from experimental data that the main challenge to discharge utilization efficiency is the prodigious loss of primary electrons to the chamber walls. The high rate of primary electron loss for this miniature discharge design was due to the need for relatively low magnetic field strengths at the boundaries that allow plasma electrons to be lost at a rate sufficient to maintain discharge stability. Investigations of this miniature discharge show that the performance is strongly coupled to the effective electron leak area of the discharge, which in turn affects the plasma stability and limits the discharge operating range.[7] From these observations, it is clear that the development of an efficient discharge of only 1 cm in diameter requires an improvement in the knowledge of the plasma dynamics and structure in the near-surface region of the cusp.

Magnetic cusp confinement of plasma at conducting surfaces involves interactions between a divergent magnetic field, multiple plasma species, and the sheath conditions near the surface.[8] Much of the research on cusp confinement has been performed using relatively larger plasma discharges with free-standing electromagnetic "picket fence" and spindle cusps far from the anode[9–12] or multi-magnet ring and line cusps for permanent magnet discharges.[13–16] These efforts have reported a "leak width" that is in contradiction of one another. Some researchers have found evidence for the leak width, w_l, on the order of electron or ion gyroradius, while the most popularly reported leak width is proportional to the hybrid gyroradius, ρ_h, such that $w_l \approx 4\rho_h = 4\sqrt{\rho_e \rho_i}$. The hybrid gyroradius is shown to be caused by ambipolar-type effects between the ions and electrons in the cusp region.

Researchers have developed computational models that can be utilized to predict electron and ion losses at the cusp. For example, a numerical code developed by Arakawa and Ishihara[17] for a cusped ion thruster predicted the losses at the cusp to be greater than experiments. In the model, plasma was treated as a fluid while assuming charge neutrality throughout the computational domain; thus, the charge separation effect in the cusp region was not incorporated. In comparison to Arakawa's model, Marcus *et al.*[18] developed a particle-in-cell (PIC) model to study plasma behavior and confinement in a picket fence magnetic cusp device. Their model assumed that all charged particles were generated in the cusp region, which is not applicable for micro-discharges. Hirakawa and Arakawa[19] developed a PIC model specifically to find the losses in magnetic cusps and showed that the model agreed qualitatively with their experimental results; however, they were unable to show quantitative agreement with the experiment. More recently, Takekida[20]

developed models for optimizing the design of a large multi-cusp confinement of a plasma discharge, but did not look closely at the physics very near the cusp.

The objective of this research is to develop a computational model to improve the understanding of cusp confinement very near the anode surface for a single permanent magnetic cusp. The expression for leak width provides a crude estimate of the leak area, but a much more accurate description is necessary to achieve our goal. Since probing of the sheath and near the cusp is extremely difficult using conventional probes, it is necessary to develop an accurate computational model of this region. This research effort is a continuation of the work presented during the 2012 Joint Propulsion Conference.[21] In that work, an electron flood gun was directed at a single cylindrical permanent magnet. Simulation results agreed well with experimental measurements, which validated a few important components of the computational model. The overall goal of this research project is to develop a 1-cm micro-ion thruster that provides a stable and efficient discharge. The knowledge gained from the effort discussed herein will be used in a hybrid fluid/PIC model that will be developed and used as a tool to design and optimize the micro-discharge. The following sections of the paper describe the details of the computational model (Sec. II) and analytical solutions for electric potential and bulk density (Sec. III). Section IV uses the analytical results to validate the model components and methodologies and provides analyses of preliminary results from the model.

II. Computational Model

A. Simulation Domain

The simulation domain is inside of a cylindrical test cell, with a conducting mesh and a plate at the boundaries (Fig. 1). The length of the test cell is determined to ensure that the primary electrons experience sufficient ionization collision with neutrals. The downstream end plate is biased at 25 V and mesh wall is grounded. Neutrals are free to escape through the mesh boundaries, while the sheath near the mesh wall prevents plasma electrons from escaping. A hollow cathode is placed along the axis, so the center of the orifice corresponds to the origin of the domain. The electrons injected from the cathode and created within the domain are confined by the magnetic field, which is created by three coils and one permanent cylindrical magnet. The magnetic cusp in front of the magnet is the region of interest. The Helmholtz coil is added to confine the primary electrons near the centerline. In addition, a coil is placed slightly upstream of the test cell in order to enhance the loss at the magnetic cusp.

B. Overview of the Computational Model

The computational model employs the iterative Monte-Carlo (MC) method, tracking super-particles of different charged species (primary electrons, ions, and plasma electrons) separately. A particle simulation is required because this effort: (1) explores densities and energies that have a large range of collisionality, and (2) seeks to resolve species interactions and dynamics in the cusp region. In the model, primary electrons are initiated from the source with a cosine distribution, whereas ions and plasma electrons are tracked from the cell-centroids assuming a Maxwellian distribution. These particles are moved in electric and magnetic

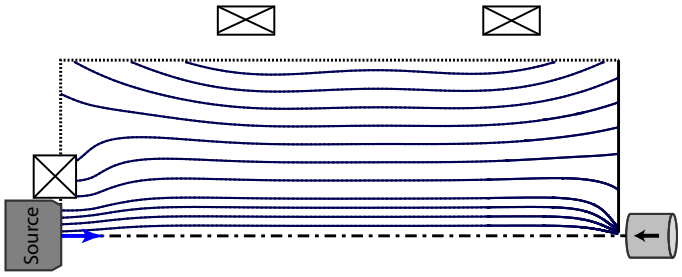

Figure 1. A slice of a cylindrical test cell to be simulated. The region of interest is in front of the cylindrical magnet placed downstream. A Helmholtz coil is used to guide the electrons near the centerline.

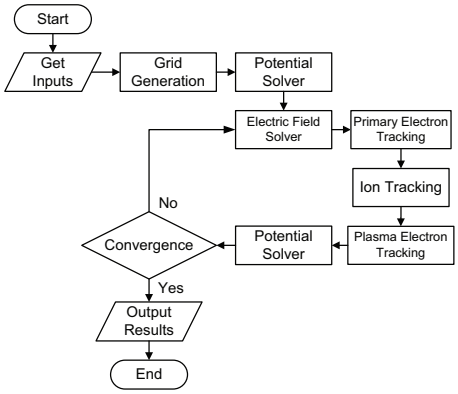

Figure 2. Simplified flowchart of the computational model.

fields while they are weighted to the computational grid at every time-step. In order to reduce the run time, the particle tracking is done in parallel using a message passing interface (MPI). Once all the particles are tracked, the electric potential and field are updated using the densities computed from the last particle tracking subroutine. These calculations are repeated until the electric potential and species densities converge (Fig. 2). Neutral density is pre-computed using the flow rate from a source and the background neutral pressure. This model can be considered as a simplified version of a particle-in-cell (PIC) model commonly used for kinetic simulations of plasma, because the electric field is computed asynchronously with particle tracking instead of being updated while the particles are tracked. The details of the numerical techniques are provided below.

C. Adaptive Cartesian Mesh

Since the Larmor radii are inversely proportional to the magnetic field strength, the spatial scale at the cusp region becomes considerably small. Therefore, a very fine mesh is necessary to resolve the high gradients in density and potential near the magnetic cusp. The computational model uses an adaptive Cartesian mesh, in which mesh refinement is increased with the magnetic field strength induced by a magnetic cusp of interest. This provides a high resolution near the magnetic cusp with a low resolution in the bulk region, which minimizes the run time without sacrificing accuracy. The mesh is generated by first creating a uniform Cartesian mesh throughout the domain and then subdividing the cells into four sub-cells. The subdivision of the cells is performed until the grid size becomes smaller than the electron gyroradius at the cusp.

D. Electric Potential and Field

For the adaptive Cartesian mesh, the standard potential calculation using three point finite difference equations provides only first-order accurate solutions at the coarse/fine grid interface while providing second-order accurate solutions for a simple rectilinear mesh. Therefore, it is necessary to use more sophisticated methods in order to keep the second order accuracy in the adaptive Cartesian mesh. The method implemented in the computational model approximates the local variation in electric potential across a cell face with the 2D quadratic spline equation.[22]

$$\phi = a_1 + a_2 z + a_3 r + a_4 z^2 + a_5 z r + a_6 r^2 \tag{1}$$

For every cell face, the six closest cells are chosen to set up six independent equations by plugging in the z and r coordinates in Eq. (1). Then, the spline coefficients can be expressed in terms of the potential of the six cells by solving the linear system of equations. In computing the electric potential, the integral form of Gauss' equation is applied to each cell by employing the finite volume method.

$$\oint_j \mathbf{E} \cdot d\mathbf{S} = -\oint_j \nabla\phi \cdot d\mathbf{S} = \frac{\rho_f V_j}{\varepsilon_0} \tag{2}$$

Using the 2D quadratic equation, the electric flux over a cell face is given as[22]

$$\begin{aligned} \int \mathbf{E} \cdot \mathbf{dS} &= -2\pi \left[\int r \frac{\partial \phi}{\partial z} dr + \int r \frac{\partial \phi}{\partial r} dz \right] \\ &= -2\pi \left[\int (a_2 + 2a_4 z + a_5 r) r dr + \int (a_3 + a_5 z + 2a_6 r) r dz \right] \end{aligned} \tag{3}$$

The surface integral given in Eq. (3) is evaluated analytically to express the electric flux in terms of potentials of the neighboring cells. Once equations for all the cells in terms of electric potential are obtained, the resulting linear system of equations is solved for the electric potentials at all the cells.

In computing the electric field, the local variation in electric potential is again expressed with the 2D quadratic equation given in Eq. (1). For a given interior cell, the number of cells neighboring the current cell range from 6 to 12, which results in an over-determined linear system of equations when solving for the spline coefficients. Therefore, the least squares approach is used to obtain a unique solution for the coefficients. The error of the quadratic equation at cell j is expressed as

$$R_j = a_1 + a_2 z_j + a_3 r_j + a_4 z_j^2 + a_5 z_j r_j + a_6 r_j^2 - \phi_j \tag{4}$$

The error of the quadratic equation through all the current and neighboring cells is minimized when the following condition is satisfied.

$$\frac{\partial R^2}{\partial a_s} = 0 \quad (s = 1 \text{ to } 6) \tag{5}$$

where $R^2 = \sum R_j^2$. Using the 6 equations from Eq. (5) and 6 unknowns, the spline coefficients can be obtained by solving the linear system of equations. Note that the same approach can be applied as long as the number of neighboring cells is greater than 5. Once the coefficients for the quadratic equation are computed, then the electric field in the current cell can be calculated by taking the gradient of Eq. (1).

E. Magnetic Field Induced by a Current Coil and a Cylindrical Magnet

The computational model utilizes analytic equations to solve magnetic fields induced by a current coil and a cylindrical permanent magnet. The use of analytic equations allows accurate determination of the magnetic field at particle locations, thus eliminating the error associated with interpolation of the fields. The magnetic field induced by a current loop is given as[23]

$$\begin{aligned} B_z &= \frac{\mu_0 I}{2\pi\sqrt{(r+r_l)^2+(z-z_l)^2}}\left[K(m)+\left(\frac{2r_l(r+r_l)}{[(r+r_l)^2+(z-z_l)^2](1-m)}-\frac{1}{1-m}\right)E(m)\right] \\ B_r &= -\frac{\mu_0 I(z-z_l)}{2\pi\sqrt{(r+r_l)^2+(z-z_l)^2}}\left[\frac{K(m)}{r}-\frac{E(m)}{r(1-m)}+\frac{2aE(m)}{[(r+r_l)^2+(z-z_l)^2](1-m)}\right] \end{aligned} \tag{6}$$

where $K(m)$ and $E(m)$ are the complete elliptic integrals of the first and second kind, respectively. The parameter, m, is the square of the elliptic modulus, and is given as $4rr_l/[(r+r_l)^2+(z-z_l)^2]$. Evaluation of Eq. (6) is relatively expensive since the equation involves elliptic integrals. Therefore, it is impractical to compute Eq. (6) for each turn of the coil. Instead, the current coil is approximated with multiple current loops that are evenly spaced within the volume of the coil. Although the approximation would not provide an accurate solution very near the coil, the magnetic field solution within the region of interest (near the centerline) is sufficiently accurate (less than 1% error with several current loops). The equation for a cylindrical parmanent magnet is obtained from an analytic equation for an axially magnetized ring magnet[24] in the limit that the inner radius approaches zero.

$$\begin{aligned} B_z &= \frac{\mu_0 M}{2\pi}\sum_{s=1}^{2}(-1)^{s-1}\Big[c_{1s}K(m_s)-c_{2s}\frac{\pi}{2}+\frac{\pi}{2}s_{1s}s_{2s}[1-\Lambda(\theta_{1s},m_s)] \\ &\qquad +\frac{\pi}{2}s_{1s}[1-\Lambda(\theta_{2s},m_s)]-\frac{\pi}{2}s_{1s}[2-\sin(\theta_{2s})-\sin(\theta_{3s})]\Big] \\ B_r &= \frac{\mu_0 M}{2\pi}\sum_{s=1}^{2}(-1)^{s}\left[\frac{a_s^2-2rr_m}{ra_s}K(m_s)-\frac{a_s}{r}E(m_s)\right] \end{aligned} \tag{7}$$

where parameters, m_s, α_s, c_{1s}, c_{2s}, θ_{1s}, θ_{2s}, θ_{3s}, s_{1s}, and s_{2s} are defined in table 1. The subscript, s, denotes the ends of the cylindrical magnet. The analytic equation for a permanent magnet is derived assuming a constant magnetization in a magnet, which is a reasonable assumption for the samarium cobalt magnets used in this study. The magnetization for a cylindrical magnet, M, is obtained by matching the axial magnetic field with the measured value at the center of the magnet face. Heuman's Lambda function, $\Lambda(\theta,m)$, given in Eq. (7) can be expressed in terms of elliptic integrals.

Table 1. Definition of parameters used in Eq. (7)

Parameter	Definition
m_s	$4rr_m/\alpha_s^2$
α_s	$\sqrt{(r+r_m)^2+(z-z_{ms})^2}$
c_{1s}	$\frac{2(z-z_{ms})\sqrt{r^2+(z-z_{ms})^2}}{\alpha_s\left(\sqrt{r^2+(z-z_{ms})}+r\right)}$
c_{2s}	$\frac{2(z-z_{ms})}{\left(\sqrt{r^2+(z-z_{ms})}+r\right)}$
h_s	$\frac{2r}{r+\sqrt{r^2+(z-z_{ms})^2}}$
θ_{1s}	$\sin^{-1}\left(\sqrt{\frac{1-h_{1s}}{1-m_s}}\right)$
θ_{2s}	$\sin^{-1}\left(\frac{\lvert z-z_{ms}\rvert}{\sqrt{r^2+(z-z_{ms})^2}+r}\right)$
θ_{3s}	$\sin^{-1}\left(\sqrt{1-h_{1s}}\right)$
s_{1s}	$\mathrm{sign}(z-z_{ms})$
s_{2s}	$\mathrm{sign}(\sqrt{r^2+(z-z_{ms})^2}-r_m)$

$$\begin{aligned} \Lambda(\theta,m) = \frac{2}{\pi}\{&K(m)E(\theta,1-m) \\ &-(K(m)-E(m))F(\theta,1-m)\} \end{aligned} \tag{8}$$

where $F(\theta,m)$ and $E(\theta,m)$ are the incomplete elliptic integrals of the first and second kind, respectively. Both Eqs. (6) and (7) contain elliptic integrals, and two different methods are used depending on the arguments. For the standard domain of elliptic

parameters, $0 < m < 1$ (and $0 < \theta < \pi/2$ for an incomplete elliptic integral), Fukushima's fast computation methods are used to evaluate complete elliptic integrals[25] and incomplete elliptic integrals of the first kind.[26] For non-standard domains of an elliptic parameter, the elliptic integrals are evaluated using the simple relationship with the elliptic integrals and Carlson's functions, R_F and R_D.[27]

$$\begin{aligned} F(\theta, m) &= \sin\theta R_F(\cos^2\theta, 1 - m\sin^2\theta, 1) \\ E(\theta, m) &= F(\theta, m) - \frac{1}{3} m \sin^3\theta R_D(\cos^2\theta, 1 - m\sin^2\theta, 1) \end{aligned} \tag{9}$$

Since the calculation of the magnetic field occurs very frequently in the computational model, accuracy and speed in evaluating the elliptic integrals are critical. Fukushima's method improved the computational time of $K(m)$, $E(m)$, and $F(\phi, m)$ by 75, 88, and 48%, respectively. This method also improved the computation time for Eq. (7) by approximately 60%.

F. Particle Tracking Method

The numerical method used to integrate the equation of motion is critical, because a large number of integrations are required by the model to determine particle trajectories. Therefore, the integration method has to be fast while remaining sufficiently accurate. In addition, the integrator method has to be able to handle high gradients in magnetic field in the cusp region. For this model, the Lorentz forces on the particles are decomposed into electric and magnetic forces in the same way as the standard Boris particle pushing technique.[29] The electrostatic force is assumed to act half at the beginning, and half at the end of a given time step. This allows the circular motion of the particle due to the magnetic field to be treated in the absence of the electric field. Consequently, the velocity after one time-step is computed in three steps.[7,28]

$$\mathbf{v}_- = \mathbf{v_n} + \left(\frac{q\Delta t}{2m}\right)\mathbf{E} \tag{10}$$

$$\mathbf{v}_+ = (\mathbf{v}_-)_\parallel + |(\mathbf{v}_-)_\perp| \left(\cos(\Delta\theta)\hat{h}_\perp - \sin(\Delta\theta)\hat{h}_\parallel\right) \tag{11}$$

$$\mathbf{v_{n+1}} = \mathbf{v}_+ + \left(\frac{q\Delta t}{2m}\right)\mathbf{E} \tag{12}$$

Here, $\hat{h}$ represents the coordinate system aligned with the magnetic field and is given below.[28]

$$\hat{h}_\parallel = \frac{\mathbf{B}}{|\mathbf{B}|}; \quad \hat{h}_\perp = \frac{\mathbf{v} - (\mathbf{v}\cdot\hat{h}_\parallel)\hat{h}_\parallel}{|\mathbf{v} - (\mathbf{v}\cdot\hat{h}_\parallel)\hat{h}_\parallel|}; \quad \hat{h}_r = \frac{q}{|q|}(\hat{h}_\parallel \times \hat{h}_\perp) \tag{13}$$

Then, the position after one time-step in the field-aligned coordinate system is given as,[7,28]

$$\begin{aligned} \Delta x_\parallel &= \Delta t(\mathbf{v}\cdot\hat{h}_\parallel)\hat{h}_\parallel \\ \Delta x_\perp &= \rho\sin(\Delta\theta)\hat{h}_\perp \\ \Delta x_r &= -\rho[1 - \cos(\Delta\theta)]\hat{h}_r \end{aligned} \tag{14}$$

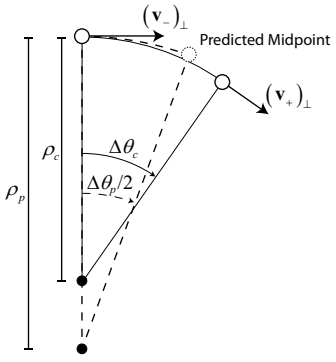

Figure 3. Illustration of predictor-corrector algorithm for integration of equation of motion.[28] The magnetic field value calculated at the midpoint is used to execute the corrected gyromotion.

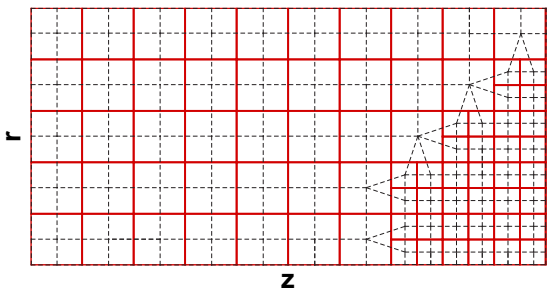

Figure 4. An example of adaptive Cartesian mesh. The solid line corresponds to cell boundaries and the dashed line corresponds to node element boundaries.

Unlike the standard method, the staggered-grid feature of the standard Boris method is removed, and position and velocity are evaluated on an aligned temporal grid. Instead, better estimations of the magnetic field are obtained by using a predictor-corrector algorithm in solving a simple circular gyromotion (Fig. 3). The predictor-corrector algorithm determines the particle trajectory for each time step by first predicting the midpoint of the trajectory assuming the magnetic field at the starting position. The magnetic field at the "predicted" midpoint is calculated and then used to determine a "corrected" final position and velocity orientation. Another important feature of the modified Boris method is that the particle rotation is executed in the magnetic field-aligned coordinate system. This feature removes the error associated with the angular displacement.

G. Particle Weighting

Particle simulation of plasma involves the exchange of information between particles and a computational grid. In particular, weighting of particles to the grid is necessary to compute the electric potential and field at discrete points, while interpolation of the field is required to obtain the electrostatic force at the particle locations. Standard weighting schemes (e.g. first order area weighting in two dimensions) work very well in Cartesian coordinates.[30] However, in cylindrical coordinates, these weighting methods produce systematic errors in particle densities at boundary nodes when a regular Cartesian mesh is used.[31–33] Furthermore, more severe systematic error occurs at the coarse/fine grid interfaces of an adaptive Cartesian mesh. In the computational model, we use the generalized weighting scheme proposed by Verboncoeur[31] in order to remove these systematic errors. The method computes particle density using a corrected cell volume calculated with the same shape factor as applied in particle weighting.

Every node element consists of 3-4 cells whose cell-center locations correspond to the vertices of the node element, as illustrated in Fig. 4. The dashed lines in Fig. 4 correspond to node element boundaries, and the intersection points of the dashed lines are the locations of the cell-centers. Once a macro-particle is determined to be within a node element, a fraction of particles are distributed to each node element vertex (cell-centroid) based on the first-order area weighting scheme. At a coarse/fine grid interface, the shape of triangular or quadrilateral element is not a right triangle or a rectangle, respectively. For this case, the weighting factor cannot be easily found in physical coordinates. Instead, the weighting factor is found in natural coordinates (Fig. 5), in which an interface element (a triangle or quadrilateral) is mapped to a reference polygon (a right triangle or square). The transformation between the two coordinates, $\xi(z,r)$ and $\eta(z,r)$, can be found using bilinear interpolation. Once the ξ and η are found for the given particle position, the number of particles assigned to a vertex, k, can be determined by,

$$N_k = N_p W_k \tag{15}$$

where the weighting factors are

$$\begin{array}{lllll} \text{Triangle:} & W_1 = 1-\xi-\eta & W_2 = \xi & W_3 = \eta & \\ \text{Quadrilateral:} & W_1 = (1-\xi)(1-\eta) & W_2 = \xi(1-\eta) & W_3 = \xi\eta & W_4 = (1-\xi)\eta \end{array} \tag{16}$$

At the end of particle tracking, the particles distributed to the boundary cells are re-assigned to the nearest interior cells, since the effective volumes of the boundary cells are essentially zero.

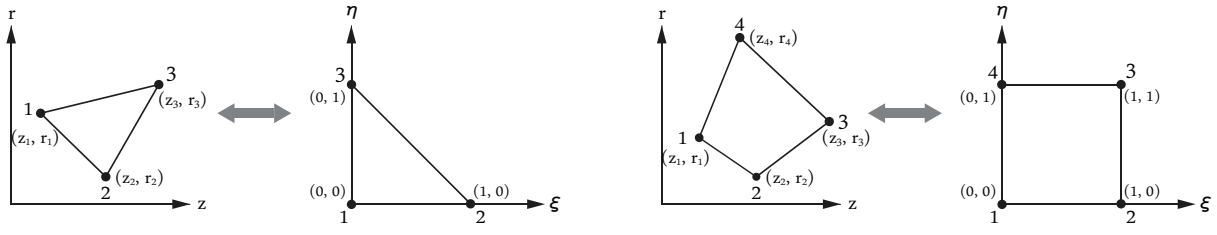

(a) Triangular element

(b) Quadrilateral element

Figure 5. Mapping of elements in natural coordinates.

In applying the generalized weighting algorithm, the particle density at the grid is calculated with the cell volume weighted using the same interpolation function applied in the particle weighting. The corrected volume calculation is also done in natural coordinates for the reference polygons. The differential volume element, dV, can be expressed in terms of natural coordinates.

$$dV = 2\pi r dz dr = 2\pi r(\xi,\eta)|J(\xi,\eta)|d\xi d\eta \tag{17}$$

where $|J(\xi,\eta)|$ is a Jacobian or a determinant of a Jacobian matrix for the mapping shown in Fig. 5.

$$[J] = \begin{bmatrix} \frac{\partial z}{\partial \xi} & \frac{\partial z}{\partial \eta} \\ \frac{\partial r}{\partial \xi} & \frac{\partial r}{\partial \eta} \end{bmatrix} \tag{18}$$

Using Eqs. (17) and (18), the corrected volume can be calculated by solving the following integrals.[34]

$$V_k = \int\int W_k(\xi,\eta) 2\pi r(\xi,\eta)|J|\, d\xi d\eta \tag{19}$$

where the limits of the integrals are $\xi = 0 \rightarrow 1-\eta$ and $\eta = 0 \rightarrow 1$ for the triangular element and $\xi = 0 \rightarrow 1$ and $\eta = 0 \rightarrow 1$ for the quadrilateral element. Simple formulas for the corrected volume calculation are provided in Ref. 35. For every node element, the weighted volumes are calculated and distributed to corresponding vertices. The sum of the volumes distributed to the same cell, V_j, is the corrected volume used for the density calculations. Again, the volumes assigned to the boundary cells are re-assigned to the nearest interior cells. Finally, using the corrected cell volumes, the particle density at cell j is computed by $n_j = N_j/V_j$.

H. Collisions

In the experiment to be simulated, the background neutral density is at least a few orders of magnitude higher than the densities of other species, and the mean free path for collisions with neutrals is much shorter than for collisions between charged species. Therefore, collisions with neutrals are incorporated in the model, which includes elastic, ionization, and excitation collisions between electrons and neutrals, as well as elastic collision between ions and neutrals. In addition to these collisions, collisions between primary and plasma electrons are incorporated by taking into account the primary electron relaxation time.[36] For ion-neutral collisions, only elastic collisions are included in the simulation. Due to the low energy of ionized particles, inelastic collisions are neglected as ions only have energies below the threshold energy of the collision. Symmetric charge-exchange collisions are also neglected because the resulting effect is similar to the elastic collision at the ion and neutral energies. For the collisions implemented in the model, curve-fit equations for different collision cross-sections are obtained from data for electron-neutral elastic,[37] ionization,[38] and excitation[39] collisions.

1. Elastic Collision

The elastic collision is approximated using the Monte Carlo collision (MCC) method. During a time-step, Δt, the probability that a particle experiences an elastic collision is expressed as

$$P_{el} = 1 - \exp(-\Delta t \sigma_{el} v n_o) \tag{20}$$

Equation (20) gives a positive value that is always less than or equal to 1. The elastic collision is assumed to take place when the condition $P_{el} > U$ is satisfied, where U is a uniformly probable number between 0 are 1 generated by the random number generator. The calculation of the post-collision velocity is done by first calculating the center of mass (CM) deflection angle and then transforming the coordinate system to determine the laboratory (LAB) frame post-collision velocity.

For an electron-neutral collision, the velocity vector after a collision is determined using a formula derived by Okhrimovskyy et al.[40] for the center of mass deflection angle calculation. Approximating the electron-neutral interaction potential by the screened Coulomb potential and using the first Born approximation of quantum scattering, an equation for determining the deflection angle can be obtained.[40]

$$\cos\chi = 1 - \frac{2U}{1 + 8\varepsilon(1-U)} \tag{21}$$

This method is only a rough approximation, but takes into account that it is more forward scattering with increasing energy. More importantly, the determination of the deflection angle is fast.

For ion-atom collision, the computational model employs variable hard sphere (VHS) model. In this model, the scattering is determined in the same way as the hard sphere model, while the cross section is determined by the following formula given by Dalgarno *et al.*[41] instead of using the physical cross section.

$$\sigma_i = \frac{64200}{v_{rel}} \text{Å}^2 \tag{22}$$

The deflection angle is given as

$$\chi = 2\cos^{-1}\sqrt{U} \tag{23}$$

Although the scattering characteristics calculated by the model are not realistic, the simple model allows fast calculations of collision mechanics.

2. Inelastic Collision

During an inelastic collision with a particle, the kinetic energy of the incident primary electron is transferred to the particle, bringing the ground energy level particle into an excited or ionized state. In a single ionization event, the primary electron lose an energy corresponding to the threshold energy of 12.13 eV. Although the primary electrons of 25 eV have a sufficient energy to experience two ionization events, it is assumed for simplicity that the primaries join the plasma electron population after an ionization event. Thus, every ionization event effectively results in one ion and two plasma electrons. In an excitation event, the kinetic energy of the primary electron is transferred into some internal mode to create an atom in an excited bound state. Similar to the ionization event, it is assumed that the primary electrons join the plasma electron population after an excitation collision. The equilibration of primary electrons interacting with the plasma electron population by Coulomb collisions is also considered, and is computed together with inelastic collisions. The equilibration rate is much faster after an inelastic collision because of the reduced energy. If this equilibration rate is faster than the rate of inelastic collision, then the assumption of a primary electron joining the plasma population after a single inelastic collision is appropriate. The change in macro-particle current due to inelastic collisions can be found using a normalized change in flux for particles, Γ, traveling a distance Δx through a density, n, of particles with collision cross-section, σ, as[42]

$$\Gamma(x + \Delta x) = \Gamma(x)\exp(-\Delta x \sigma n) \tag{24}$$

The effective product of density and collision cross-section can be approximated by

$$\sigma n = n_o\left(\sigma_{iz} + \sigma_{ex}\right) + n_{se}\sigma_{slow} \tag{25}$$

The amount of representative current loss during the time step due to ionization is added to the volumetric ionization rate of the local cell by

$$\dot{n}_{iz} = \frac{J\left(1 - \exp(-\Delta x \sigma_{iz} n_o)\right)}{V_j} \tag{26}$$

By computing the ionization and excitation rate within the local cell, the volumetric generation rate of ions and plasma electrons can be determined.

I. Convergence

The convergence of the solution is determined by the change in the electric potential and species densities between the iterations. For the electric potential, the total deviation between the iterations is given by

$$||\delta\phi||_2 = \sqrt{\frac{\sum_j^{N_c}\left(\phi_j^{k+1} - \phi_j^k\right)^2}{\sum_j^{N_c}\left(\phi_j^{k+1}\right)^2}} \tag{27}$$

Similar equations are also used for species densities. When the total deviations for potential and species densities are all smaller than a chosen tolerance, ϵ, specified as an input, then the solution is considered to be converged.

Although the computational model in this study is inherently faster in finding the steady-state solution compared to the regular PIC models, it is difficult to obtain a converged solution with an iterative Monte-Carlo method. In the model, ion and secondary electron trajectories are determined separately. In other words, all the ions are tracked before secondary electrons. Consequently, the low-energy species over-react to the small changes in the potential, and the maximum potential value oscillates between very large and small values because of the opposite charge of the two species. For this reason, we implemented a few techniques to enhance the convergence of the solution. First, the change in particle density is limited so that the computed particle density, n^k_{out}, obtained from particle tracking cannot be greater than $10n^k$. This prevents over-shoot of the solution between iterations. Then, the values of the electric potential are scaled so the volume-averaged value is below 50 V. This prevents large potential gradients and slow particles from over-reacting by the electric field. Once the potential solution approaches close enough to the expected solution, the potential scaling is turned off. Finally, the computed electric potential and species densities are mixed with the values obtained from several previous iterations.

$$n^{k+1} = \frac{1}{Q+1}\frac{\sum_{m=k-Q}^{Q} n^m_{out}}{Q} + \frac{Q}{Q+1}\frac{\sum_{m=k-Q}^{Q} n^m}{Q} \tag{28}$$

In the simulation, densities from 25 previous iterations ($Q = 25$) are used in Eq. (28). In addition, quasi-neutrality is enforced by adjusting the plasma electron density when the density is large enough such that the debye length becomes smaller than the dimension of the grid cell, L_j.

$$\lambda_{D,j} = \sqrt{\frac{\varepsilon_0 T_{e,j}}{n_{e,j} q}} < \frac{1}{2} L_j \tag{29}$$

If this condition is satisfied, plasma electrons should be able to shield the field caused by ions within a cell. The enforcement of quasi-neutrality in some region is found to be needed as a slight charge imbalance ($n_{\text{total}} \sim \pm 10^{16} m^{-3}$) causes the over-shoot in potential solution.

III. Analytical Description for Model Validation

A. Electric Potential and Field for Downstream End Plate Biased at a Fixed Potential

The analytical solutions obtained for electric potential and field are obtained for the simulation domain described in Sec. II.A. These solutions are compared with the computational results to validate the components of the model. When there is no plasma species present in the domain, the electric potential solution can be derived by solving the Laplace equation in cylindrical coordinates.

$$\nabla^2 \phi(r,\theta,z) = \frac{1}{r}\frac{\partial \phi}{\partial r} + \frac{\partial^2 \phi}{\partial r^2} + \frac{1}{r^2}\frac{\partial \phi}{\partial \theta} + \frac{\partial^2 \phi}{\partial z^2} = 0 \tag{30}$$

The general solutions for the Laplace equation is obtained by using separation of variable.[43]

$$\begin{aligned}\phi(r,\theta,z) = \sum_{m=0}^{\infty}\sum_{n=1}^{\infty} &\left[A_{mn} J_m(k_n r) + B_{mn} Y_m(k_n r)\right] \\ &\times \left[C_{mn}\sin(m\theta) + D_{mn}\cos(m\theta)\right]\left[E_{mn}\sinh(k_n z) + F_{mn}\cosh(k_n z)\right]\end{aligned} \tag{31}$$

or

$$\begin{aligned}\phi(r,\theta,z) = \sum_{m=0}^{\infty}\sum_{n=1}^{\infty} &\left[A_{mn} I_m(k_n r) + B_{mn} K_m(k_n r)\right] \\ &\times \left[C_{mn}\sin(m\theta) + D_{mn}\cos(m\theta)\right]\left[E_{mn}\sin(k_n z) + F_{mn}\cos(k_n z)\right]\end{aligned} \tag{32}$$

where A, B, C, D, E, and F are some constants, J_m and Y_m are the mth order Bessel function of the first and second kind, I_m and K_m are the mth order modified Bessel function of the first and the second kind, k_n is constant, and m and n are integers. For given boundary conditions, Eq. (31) is the appropriate general solution to be used. Applying boundary conditions and axisymmetry of the domain, Eq. (31) is simplified as

$$\phi(r,z) = \sum_{n=1}^{\infty} G_n \sinh(k_n z) J_0(k_n r) \tag{33}$$

where G_n are constants, k_n is determined by setting $J_0(k_n a) = 0$ which corresponds to $k_n a$=2.4048, 5.5201, 8.6537, $\cdots$, and a is the radius of the domain. G_n can be determined using orthogonal property of J_0 and sinh functions.

$$G_n = \frac{2V_0}{k_n a J_1(k_n a)\sinh(k_n L)} \tag{34}$$

The analytical solution for the electric field can be computed by simply taking the gradient of Eq. (33).

$$\begin{aligned} E_z(r,\theta,z) &= -\sum_{n=1}^{\infty} k_n G_n \cosh(k_n z) J_0(k_n r) \\ E_r(r,\theta,z) &= \sum_{n=1}^{\infty} k_n G_n \sinh(k_n z) J_1(k_n r) \end{aligned} \tag{35}$$

where J_1 is the first order Bessel function of the first kind. Equations (33) and (35) involve infinite sum of hyperbolic and Bessel functions. The infinite sum is truncated at n =1,000; this number is determined so that the solution is obtained within a reasonable amount of time with sufficient accuracy. Figure 6 shows a plot of potential contour; red corresponds to 25 V and blue corresponds to 0 V. Even with a large number of terms for the infinite sum used to compute the solution, the lower accuracy at the circumference of the end plate is inevitable because of the sudden change of the boundary condition from the end plate to the cylinder wall. Therefore, the solutions are only compared within the dashed box shown in Fig. 6.

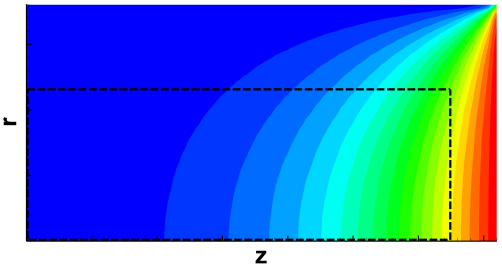

Figure 6. Contour plot of potential (V) calculated with the analytical solution for the case with a cylindrical domain with end plate biased at 25 V. Red corresponds to 25 V and blue corresponds to 0 V. The solutions are compared for the cells inside the dashed box.

B. Radial Bulk Density Profile

A simple analytical model is developed to approximate the density profile along the radius. The result from the analytical model described herein is compared with the computational result for model validation. The density profile along the radius can be estimated with the diffusion equation.

$$\frac{\partial n}{\partial t} - D\nabla^2 n = \dot{n}(r) \tag{36}$$

The first term in Eq. (36) is neglected since the solution of interest is steady-state. In this formulation, it is assumed that the magnetic field is homogeneous away from the magnetic cusp in the direction parallel to the axis. Assuming that the ion generation rate density profile along the radius can be expressed by a polynomial of degree N_d, the equation to be solved becomes,

$$-D_\perp \frac{1}{r}\frac{\partial}{\partial r}\left(r\frac{\partial n}{\partial r}\right) = \dot{n}(r) = \sum_{s=1}^{N_d} p_s r^{N_d - s} \tag{37}$$

where p is the polynomial coefficients. At the edge of the sheath near the side wall, the characteristic loss velocity of ions, u_w is assumed to satisfy the Bohm criterion for a positive sheath, $u_w = u_{Bohm} = \sqrt{kT_e/m_i}$. Thus, the boundary conditions are,

$$n(r = r_{max}) = n_w, \quad \Gamma = -D_\perp \left.\frac{\partial n}{\partial r}\right|_{r=r_{max}} = n_w u_w \tag{38}$$

The solution of Eq. (37) is then,

$$n(r) = \sum_{s=1}^{N_d} \frac{p_s}{(N_d - s + 2)^2}\left[\frac{r_{max}^{(N_d - s + 2)} - r^{(N_d - s + 2)}}{D_\perp} + \frac{r^{(N_d + s + 1)}}{u_w}(N_d - s + 2)\right] \tag{39}$$

A similar solution can be derived using a boundary condition with $n(r = r_{max}) = 0$, yielding Eq. (39) without the second term in the parentheses. Equation (39) is dependent on the perpendicular diffusion coefficient, $D_\perp$, which is difficult to obtain for our specific problem. The classical ambipolar diffusion across a magnetic field can be obtained by equating the ion and electron fluxes perpendicular to the direction of magnetic field.[44]

$$D_\perp = \frac{\mu_{i\perp} D_{e\perp} - \mu_{e\perp} D_{i\perp}}{\mu_{i\perp} - \mu_{e\perp}} \tag{40}$$

The diffusion coefficient given in Eq. (40) is appropriate in a infinitely long cylindrical plasma with uniform magnetic field along the axis. When the domain is finite and is bounded by conducting walls, the diffusion coefficient should be modified to take into account of Simon's "short-circuit" effect.[45]

$$D_\perp = \frac{\mu_i D_{e\perp} - \mu_e D_{i\perp}}{\mu_i - \mu_e} \tag{41}$$

Unlike the case with the classical ambipolar diffusion, the particle flux is no longer at the same equilibrium value in each direction, but rather the total flux for each species should be maintained. In our problem, strong and weak cusps are placed at the downstream and upstream ends, respectively. In this magnetic field configuration, electrons are not freely lost to the ends if they are confined near the centerline. In contrast, the electrons are easily lost at the ends away from the centerline due to the low field strength. Therefore, the diffusion coefficient applicable for our problem is likely between Eq. (40) and Eq. (41), and the density solutions obtained using the two diffusion coefficients should provide the upper and lower bounds for the computational result.

IV. Results and Discussion

A. Validation of Weighting Scheme

The particle weighting algorithm implemented in the computational model is tested by applying a uniform current density distribution from the upstream end of the cylindrical domain.[35] Macro-particles are advanced in a direction perpendicular to the downstream end while the particles are weighted to the cells using area weighting for each time-step. If the generalized weighting scheme is applied properly, the density distribution should be uniform throughout the computational domain. Figure 7 shows the normalized density computed using the uncorrected and the corrected cell volumes, respectively. The results are obtained with $1,000,000$ macro-particles and $2,000$ time-steps before reaching the downstream end. In Fig. 7(a), the errors at top and bottom cells apart from the grid interface are 8.3 and 0.93 percent, respectively. The errors at those cells can be predicted from the ratio of the corrected volume to the uncorrected volume. At the grid interface, the error becomes more severe, reaching a value greater than 45 percent. These systematic errors are reduced significantly by using the corrected volumes as shown in Fig. 7(b). The systematic errors at the top and bottom cells are eliminated almost completely with errors of less than 0.007 percent, similarly to the results shown in Ref. 31 for one dimensional radial grid. Furthermore, the densities at cells along the grid interface match the theoretical values.

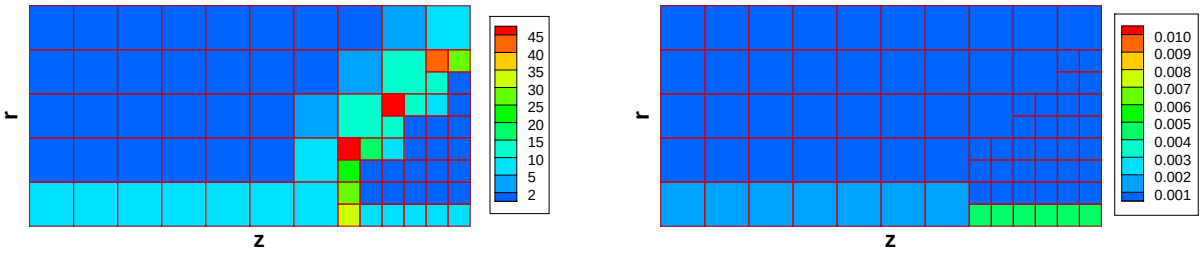

(a) Standard method

(b) Generalized Weighting Scheme

Figure 7. Percent relative error in density computed at cell centroids.[35]

B. Validation of Electric Potential and Field Solver

Figures 8 and 9 show the relative errors for the electric potential and field solutions, respectively, computed by (a) the standard methods and (b) the methods implemented in the model. The standard methods produce relatively larger errors at the cells near the coarse/fine grid interface. These errors are removed when using the refined methods implemented in the model (Fig. 8 for potential and Fig. 9 for electric field). As seen in Fig. 10, the standard methods provide second-order accurate solutions when using a uniform mesh. However, the order of accuracy drops by one order for an adaptive mesh. The accuracy is recovered when using the refined methods implemented in the computational model. In addition, examining Fig. 9(a), smaller errors are found in the region of finer mesh size, indicating that a very accurate electric potential and field solution near the cusp can be expected if the species densities are accurate.

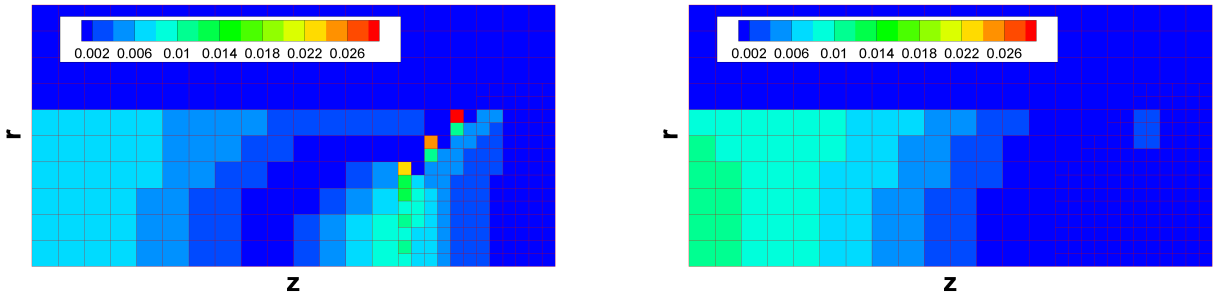

(a) Standard method (b) Spline method

Figure 8. Plot of relative error in potential solution.

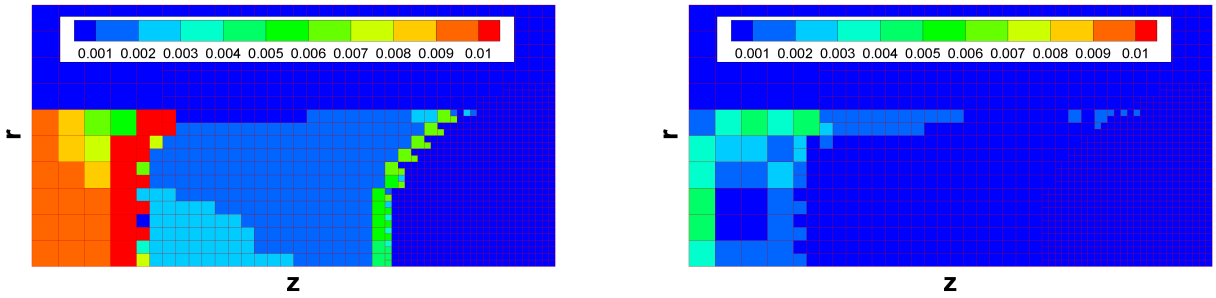

(a) Standard method (b) Least squares method

Figure 9. Plot of relative error in electric field solution.

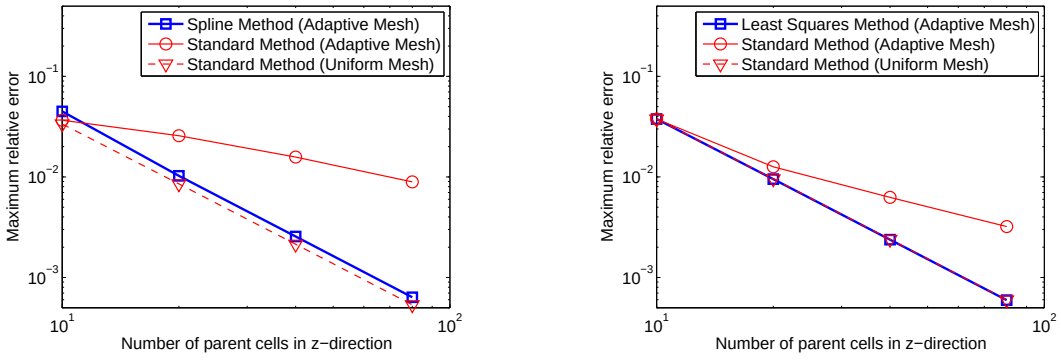

(a) Electric potential (b) Electric field

Figure 10. Convergence of electric potential and field solutions.

C. Test Simulation for Cusp-Confined Weakly Ionized Plasma

Preliminary results are obtained for the domain described in Sec. II.A. In this simulation, the hollow cathode with orifice of 1 mm in radius is assumed to operate at 0.4 A discharge current. At the exit of the cathode, it is also assumed that mono-energetic (8 eV) primary electrons enter the domain uniformly with a cosine distribution for their velocity directions. The neutral flow rate through the hollow cathode orifice is 0.6 sccm. The flow rate and the background chamber pressure of 3 mTorr are used to compute the neutral density (Fig. 11). The neutral density is assumed to remain constant throughout the simulation since the ion density is a few orders of magnitude lower than the neutral density and the reduction in neutral density due to ionization collision is insignificant. Unfortunately, the solution did not converge at the end of simulation as shown in Fig. 12 and 13. The species densities were nearly steady-state, but the ion and plasma electron densities were still changing near the end of simulation. Note that simulation was restarted at iteration of 163, and ceiling and scaling of potential for convergence enhancement was turned off. The electric potential was far from convergence; the max potential was at > 200 V, while we expected that the maximum and volume averaged potential to be close to the expected plasma potential of ~ 33 V.

Figure 14 compares the computational and analytical results for a density profile along the radius at $z = z_{max}/2$. The profile for ion generation rate density is obtained by the computational model and is fitted with a polynomial of degree $N_d = 9$. As seen in Fig. 14, the computational result does not agree well with the analytical solution; we expected that the computational result would be bounded by the profiles predicted using ambipolar and Simon's diffusion coefficients. One of the reasons for the disagreement may be that the electric potential has not been developed completely at the end of simulation. For the profile shown in Fig. 14, a converged solution for the electric field is expected to act to push the ions near the centerline further radially outward, so the density profile is flattened. Comparing the computational results in the middle and at the end of simulation, the slope of the density profile became closer to the analytical solution; however, further iterations did not result in the expected density profile. Another source of the error can be the finite dimension of the domain. The transport in the axial direction is neglected in the analytical model; however, a finite diffusion in axial direction must be present even at $z = z_{max}/2$ since the domain radius is only a third of the length. The computational model predicted slight variation of density axially near the axis while relatively larger density variation was seen further away from the axis. Finally,

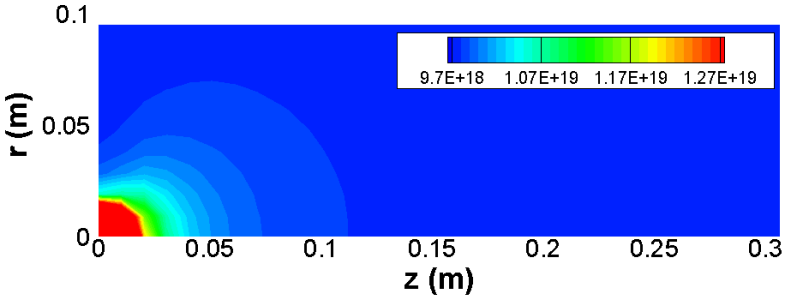

Figure 11. Contour plot of neutral density (m^{-3}). The highest neutral density is at the origin with the density of $> 2.2 \times 10^{19}$ m^{-3}.

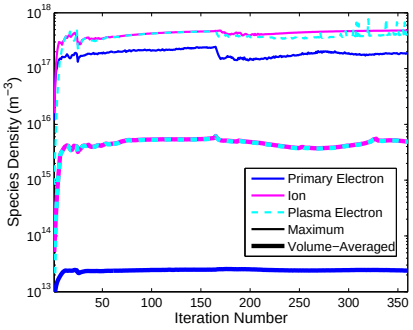

Figure 12. Maximum and volume averaged densities vs. Iteration. The densities were mixed with values from 25 previous iterations.

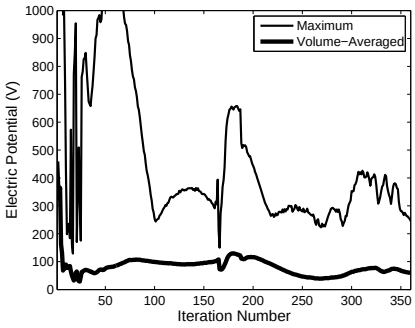

Figure 13. Maximum and volume-averaged electric potential vs. Iteration. The values were obtained directly from potential solver (before performing mixing with potential values from 25 previous iterations).

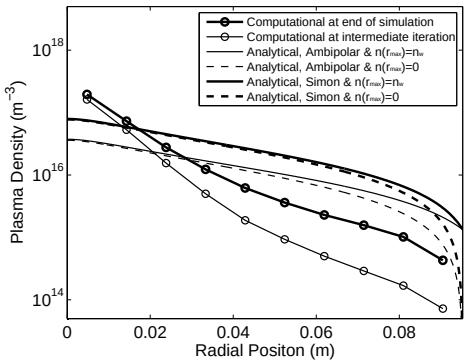

Figure 14. Comparison of density profile along the radius at $z = z_{max}/2$.

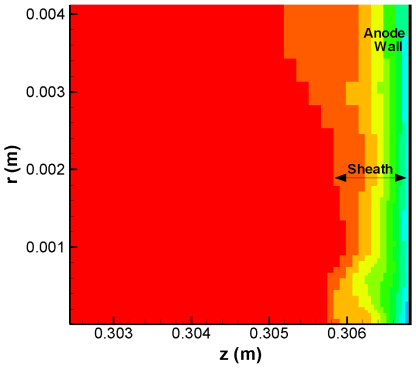

Figure 15. Electric potential near the anode wall at the magnetic cusp. Magnet face is at $z = 0.31$ m. Sheath is developed along the anode wall.

azimuthal inertia terms in the diffusion equation are neglected in the analytical formulation which may be significant.

Since the solution did not converge at the end of the simulation, the results are inaccurate but do exhibit some physical consistencies when comparing the potential structure and the relative species density distributions. Figure 15 shows the potential structure near the cusp. The contour level is omitted as the magnitude is not of importance here, but red corresponds to high potential and blue corresponds to low potential. It is clearly seen that there is a sheath along the anode wall as represented by the steep drop of the potential toward the wall. Figure 16 compares the species densities near the cylindrical magnet cusp. The right hand side of the domain shown in Fig. 16 represents the anode wall at the magnetic cusp; the magnet face is 3 mm downstream of this surface. The general and relative structure of the density profiles shown in these plots remained unchanged toward the end of simulation. Since the hollow cathode is placed along the same axis as the cylindrical magnet, the primary electrons are directed toward the cusp and are confined very near the centerline. Primary electrons are not as confined by magnetic mirroring and sheath as plasma electrons, so the residence time of primary electron is a few orders of magnitude less than that of plasma electron. Therefore, it is much more difficult for the primary electrons to diffuse across the magnetic field. Because of the concentrated primary electron population near the centerline, the potential is developed to attract ions radially inward. The radial component of the electric field interacts with the axial magnetic field to create an azimuthal E×B drift for the highly confined secondary electrons. Ions and plasma electrons are predominately created by inelastic collisions between primary electrons and neutrals, so their generation

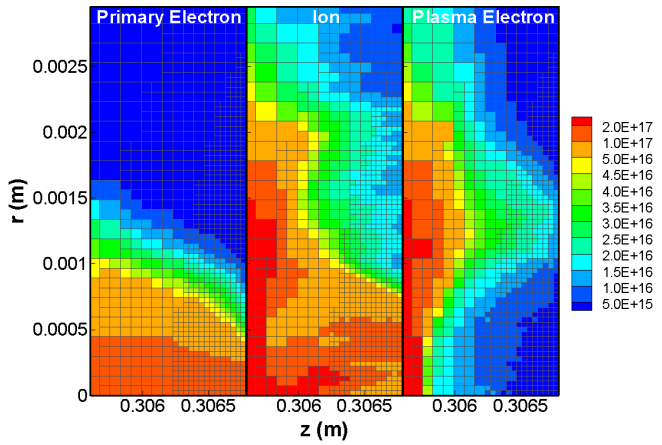

Figure 16. Species densities (m^{-3}) very near the cusp. Magnet face is at $z = 0.31$ m. Primary electrons are confined very near the centerline.

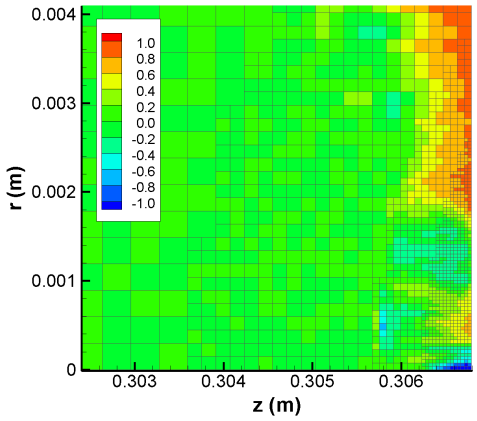

Figure 17. Degree of quasi-neutrality obtained by $\eta = (n_i - n_e)/\max(n_i, n_e)$. Magnet face is at $z = 0.31$ m. Positive and negative contours indicate regions dominated by ions and electrons, respectively.

rate density is high in the region of high primary electron density. Ions created very near the magnetic cusp are immediately accelerated toward the wall whereas plasma electrons are repelled from the wall. As the plasma electrons are strongly confined by the magnetic field and sheath, these preliminary results suggest that their path length is to be over 50 times longer than that for primary electrons. The plasma electrons diffuse much further radially outward due to multiple elastic collisions with neutrals and eventually gain enough parallel velocity to reach the anode wall. As a result, it appears that they are mainly collected in an annular region surrounding the axis near the cusp. Consequently, these preliminary results suggest that in the near-sheath and sheath region near the axis may be dominated by the primary electrons and ions while the plasma electrons and ions occupy the outer region at low primary electron density. These results do not agree with measurements in spindle cusp and picket fence experiments[9–12] and may be attributable in part to the current lack of a converged solution. We wish to note, however, that in contrast to the experiments mentioned the cusp here occurs at a current collecting wall. The electric field at the wall must be such that a sufficient current of electrons is drawn to maintain the discharge. If the electron current near the cusp is ample, one may expect the normal sheath formation as electrons are lost rapidly along the field lines. The different boundary conditions here may reasonably be expected to result in different distributions.

Figure 17 shows the local degree of quasi-neutrality, η, obtained by the computational result where η is given as,

$$\eta = \frac{n_i - n_e}{\max(n_i, n_e)} \tag{42}$$

Here, $\eta = 0$, $\eta > 0$, and $\eta < 0$ indicate quasi-neutral, ion-dominated, and electron-dominated, respectively. As shown in Fig. 17, ions dominate the near-wall region at $r \gtrsim 1.6$ mm. This is, again, due to the sheath potential that accelerate ions toward the wall and repel plasma electrons away from the wall. Within the near-wall region at $r \lesssim 1.6$ mm, the positive sheath is still present, but the difference between the plasma and anode potential is not large enough to prevent primary electrons from being lost at the wall. As a result, ions in this simulation respond to the potential structure caused by the high primary electron concentration. However, they do not reside in the region long enough to completely counteract charge imbalance, being accelerated toward the wall by the sheath. Therefore, the region very near the centerline is dominated by the primary electrons.

V. Conclusion

The iterative Monte-Carlo model has been developed to examine the species loss mechanism and plasma structure very near the magnetic cusp created by a single cylindrical magnet. The model utilizes an adaptive Cartesian mesh and refined methods for potential calculation and particle weighting in order to resolve the charge separation effect within the small region at the cusp. The model also uses analytic equations for magnetic field and a modified Boris method to accurately predict the species trajectories.

The methods implemented in the computational model for computing electric potential and field were validated against the analytical solution for the case with a cylindrical domain with the downstream end biased at a fixed potential. It was shown that the computational model provided the second-order accurate solutions even at the coarse/fine grid interface of an adaptive mesh. The particle weighting algorithm implemented in the model was also validated by a simple test case with uniform current density distribution along the radius. The errors seen when using the standard area-weighting scheme were reduced by several orders of magnitude. Finally, the computational model was used to perform a preliminary simulation for a cusp-confined weakly ionized plasma. Although the model did not provide fully converged results, it was still capable of show a sheath structure and providing interesting results for the plasma species distribution very near the magnetic cusp.

The current version of the computational model has yet to provide convergence for the simulated conditions, so much refinement to the model is still necessary. The most important improvement to be made is for the solution convergence. One modification to the current version can be the use of more sophisticated iteration mixing techniques. In addition to the convergence, a few simplifications made in the model should be updated to represent more accurate physics. For example, the primary electrons are assumed to be mono-energetic. Instead, we can implement a velocity distribution that is more accurate for the cathode being used in the experiment. Finally, secondary electron emission from the anode surface should be implemented.

Acknowledgments

The authors thank the AFOSR Young Investigator Program (YIP) Grant FA9550-11-1-0029 and University of California, Los Angeles for supporting this research. The authors also thank Ben Dankongkakul and Dr. Taylor Matlock for helpful discussions.

References

[1]Conversano, R. and Wirz, R. E., "CubeSat Lunar Mission Using a Miniature Ion Thruster," *47th AIAA/ASME/SAE/ASEE Joint Propulsion Conf. & Exhibit*, San Diego, California, 2011, AIAA 2011-6083.

[2]Wirz, R. E., Mueller, J., Gale, M., and Marrese, C., "Miniature Ion Engines for Precision Formation Flying," *40th AIAA/ASME/SAE/ASEE Joint Propulsion Conf. & Exhibit, Ft. Lauderdale, Florida*, 2004, AIAA 2004-4115.

[3]Martin, S., Scharf, D., Wirz, R. E., Lay, O., McKinstry, D., Mennesson, B., Purcell, G., Rodriguez, J., Scherr, L., Smith, J. R., and Wayne, L., "Design Study for a Planet-Finding Space Interferometer," *Proceedings of IEEE Aerospace Conference*, Big Sky, Montana, 2008.

[4]Wirz, R. E., Anderson, J. R., Goebel, D. M., and Katz, I., "Decel Grid Effects on Ion Thruster Grid Erosion," *IEEE Transactions on Plasma Science*, Vol. 36, No. 5, October 2008, pp. 2122–2129.

[5]Goebel, D. M., Wirz, R. E., and Katz, I., "Ion Thruster Discharge Performance Model," *Journal of Propulsion and Power*, Vol. 23, No. 5, 2007, pp. 1055–1067.

[6]Wirz, R. E., Polk, J., Marrese, C., Mueller, J., Escobedo, J., and Sheehan, P., "Experimental and Computational Investigation of the Performance of a Micro-Ion Thruster," *38th AIAA/ASME/SAE/ASEE Joint Propulsion Conf. & Exhibit, Indianapolis, Indiana*, 2002, AIAA 2002-3835.

[7]Wirz, R. E., *Discharge Plasma Processes of Ring-Cusp Ion Thrusters*, Ph.D. thesis, California Institute of Technology, Pasadena, CA, 2005.

[8]Martinez-Sanchez, M. and Ahedo, E., "Magnetic Mirror Effects on a Collisionless Plasma in a Convergent Geometry," *Physics of Plasmas*, Vol. 18, No. 033509, 2011.

[9]Hershkowitz, N., Leung, K. N., and Romesser, T., "Plasma Leakage through a Low-Beta Line Cusp," *Physical Review Letters*, Vol. 35, No. 5, 1975, pp. 277–280.

[10]Leung, K. N., Hershkowitz, N., and MacKenzie, K. R., "Plasma Confinement by Localized Cusps," *Physics of Fluids*, Vol. 19, No. 1045, 1976.

[11]Bosch, R. A. and Merlino, A. W., "Confinement of a potassium plasma in a spindle cusp magnetic field," *Journal of Applied Physics*, Vol. 60, No. 3056, 1986.

[12]Bosch, R. A. and Merlino, A. W., "Confinement Properties of a Low-Beta Discharge in a Spindle Cusp Magnetic Field," *Physics of Fluids*, Vol. 29, No. 1998, 1986.

[13]Christensen, T., Hershkowitz, N., and Leung, K. N., "Mass Scaling of Permanent Magnet Line Cusp Plasma Leaks," *IEEE Transactions on Plasma Science*, Vol. PS-5, No. 1, March 1977.

[14]Jones, R., "A Source of Error in Cusp Plasma Leak Measurements," *Plasma Physics*, Vol. 21, No. 505, 1979.

[15]Matlock, T., Lozano, P., and Martinez-Sanchez, M., "Discharge Chamber Wall Flux Measurements in a Diverging Cusped-Field Thruster," *ESA/A3F Space Propulsion Conference*, San Sebastian, ES, May 2010.

[16]Hubble, A. A. and Foster, J. E., "Spatially Resolved Study of Primary Electron Transport in Magnetic Cusps," *Journal of Vacuum Science Technology A*, Vol. 30, 2012, pp. 011301.

[17]Arakawa, Y. and Ishihara, "A Numerical Code for Cusped Ion Thrusters," *22nd International Electric Propulsion Conference, Viareggio, Italy*, Oct. 1991, IEPC–91–118.

[18]Marcus, A. J., Knorr, G., and Joyce, G., "Two-Dimensional Simulation of Cusp Confinement of a Plasma," *Plasma Physics*, Vol. 22, 2000, pp. 1015–1027.

[19]Hirakawa, M. and Arakawa, Y., "Plasma Particle Simulation in Cusped Ion Thrusters," *24th International Electric Propulsion Conference, Moscow, Russia*, Sep 1995, IEPC–93–242.

[20]Takekida, H. and Nanbu, K., "Particle Modeling of Plasma Confinement by a Multipolar Magnetic Field," *Journal of Physics D: Applied Physics*, Vol. 37, 2004, pp. 1800–1808.

[21]Wirz, R. E., Araki, S. J., and Dankongkakul, B., "Near-Surface Cusp Confinement for Weakly IOnized Plasma," *48th AIAA Joint Propulsion Conference, Atlanta, GA*, 2012, AIAA 2012-3948.

[22]Fox, J. M., *Advances in Fully-Kinetic PIC Simulations of a Near-Vacuum Hall Thruster and Other Plasma Systems*, Ph.D. thesis, Massachusetts Institute of Technology, 2007.

[23]Kuns, K., "Calculation of Magnetic Field Inside Plasma Chamber," Tech. rep., UCLA, 2007.

[24]Babic, S. and Akyel, C., "Improvement in the analytical calculation of the magnetic field produced by permanent magnet rings," *Progress In Electromagnetics Research*, Vol. 5, 2008, pp. 71–82.

[25]Fukushima, T., "Fast Computation of Complete Elliptic Integrals and Jacobian Elliptic Functions," *Celestial Mechanics and Dynamical Astronomy*, Vol. 105, No. 4, 2009, pp. 305–328.

[26]Fukushima, T., "Fast Computation of Incomplete Elliptic Integral of First Kind by Half Argument Transformation," *Numerische Mathematik*, Vol. 116, No. 4, 2010, pp. 687–719.

[27]Press, W. H., Teukolsky, S. A., Vetterling, W. T., and Flannery, B. P., *Numerical Recipes in FORTRAN: The Art of Scientific Computing*, Cambridge University Press, Cambridge, 2nd ed., 1992.

[28]Mao, H.-S. and Wirz, R. E., "Comparison of Charged Particle Tracking Methods for Non-Uniform Magnetic Fields," *42nd AIAA Plasmadynamics and Lasers Conference*, Honolulu, Hawaii, June 2011, AIAA 2011-3739.

[29]Boris, J. P., "Relativistic Plasma Simulations-Optimization of a Hybrid Code," *Proceedings of the 4th Conference of Numerical Simulation of Plasmas*, Washington DC, 1970.

[30]Birdsall, C. K. and Langdon, A. B., *Plasma Physics via Computer Simulation*, IOP Publishing Ltd., 1991.

[31]Verboncoeur, J., "Symmetric Spline Weighting for Charge and Current Density in Particle Simulation," *Journal of Computational Physics*, Vol. 174, No. 1, November 2001, pp. 421–427.

[32]Larson, D., Hewett, D. W., and Langdon, A. B., "Correction Factors for PIC Accumulation on Radial Grids," *Computer Physics Communications*, Vol. 90, October 1995, pp. 260–266.

[33]Ruyten, W., "Density-Conserving Shape Factors for Particle Simulations in Cylindrical and Spherical Coordinates," *Journal of Computational Physics*, Vol. 105, No. 2, April 1993, pp. 224–232.

[34]Vazquez, P. A. and Castellanos, A., "Weighting of Charge in PIC Codes for Unstructured Meshes in Cylindrical Coordinates: Application to Charged Jets," *IEEE Conf. on Electrical Insulation and Dielectric Phenomena, Nashville, Tenessee*, 2005.

[35]Araki, S. J., "Particle Weighting Algorithm for PIC Simulations in a Non-Uniform 2D Axisymmetric Mesh," *Journal of Computational Physics*, Submitted for publication.

[36]Spitzer, L. J., *Physics of Fully Ionized Gases*, Interscience, New York, 2nd ed., 1962.

[37]Hayashi, M., *Bibliography of Electron and Photon Cross Sections with Atoms and Molecules Published in the 20th Century: Xenon*, National Institute for Fusion Science (Japan), 2003, NIFS-DATA-72.

[38]Rapp, D. and Englander-Golden, P., "Total Cross Sections for Ionization and Attachment in Gases by Electron Impact: I. Positive Ionization," *Journal of Physics B: Atomic, Molecular and Optical Physics*, Vol. 43, No. 5, 1965, pp. 1464–1479.

[39]Hayashi, M., "Determination of Electron-Xenon Total Excitation Cross-Sections, from Threshold to 100 eV, from Experimental Values of Townsend's α," *Journal of Physics D: Applied Physics*, Vol. 16, 1983, pp. 581–589.

[40]Okhrimovskyy, A., Bogaerts, A., and Gijbels, G., "Electron Anisotropic Scattering in Gases: A Formula for Monte Carlo Simulations," *Physical Review E*, Vol. 65, No. 037402, 2002.

[41]Dalgarno, A., McDowell, M. R. C., and Williams, A., *Philosophical Transactions of the Royal Society of London. Series A, Mathematical and Physical Science*, Vol. 250, No. 982, 1958, pp. 411–425.

[42]Chen, F. F., *Introduction to Plasma Physics and Controlled Fusion Volumn 1: Plasma Physics*, Springer, New York, 2nd ed., 2006.

[43]Jackson, J. D., *Classical Electrodynamics*, Wiley, New York, 3rd ed., 1999.

[44]Krall, N. A. and Trivelpiece, A. W., *Principles of Plasma Physics*, McGraw-Hill, Inc, New York, 1973.

[45]Simon, A., "Ambipolar Diffusion in a Magnetic Field," *Physical Review*, Vol. 98, Apr 1955, pp. 317–318.